Cellular and Molecular Life Sciences (2025) 82:115
https://doi.org/10.1007/s00018-025-05620-0

Cellular and Molecular Life Sciences

ORIGINAL ARTICLE

Identification of early genes in the pathophysiology of fibrotic interstitial lung disease in a new model of pulmonary fibrosis

Nathan Hennion[1] · Corentin Bedart[1] · Léonie Vandomber[1] · Frédéric Gottrand[1] · Sarah Humez[2,3] · Cécile Chenivesse[4] · Jean-Luc Desseyn[1] · Valérie Gouyer[1]

Received: 19 September 2024 / Revised: 5 February 2025 / Accepted: 10 February 2025

Abstract

Some interstitial lung diseases involve pulmonary fibrosis, which is a process that is characterized by the excessive and abnormal accumulation of extracellular matrix in the pulmonary interalveolar space. Although the current anti-fibrotic therapy aims at slowing down the progression of pulmonary fibrosis, it does not reverse it, and many of the drugs that were identified in basic-research studies failed in clinical phases, mainly because of the lack of a model that can recapitulate the pathophysiological mechanisms of human pulmonary fibrosis. We developed a novel experimental model of pulmonary fibrosis induced by a cocktail of molecules on an air/liquid interface culture of mouse embryonic lung explants. Histological analyses revealed a pattern of usual interstitial pneumonia, the worst-prognosis form of pulmonary fibrosis. We performed a transcriptomics analysis at the single-cell level after the induction of fibrosis and before any histological signs of fibrosis could be observed. The results revealed increased expression of several gene families that are involved in early inflammation, fibrosis and iron homeostasis, as well as potential new genetic targets.

Keywords Mouse · Embryo · Lung · Explant · Single-cell RNA-sequencing

Introduction

The interstitial lung disease (ILD) family encompasses disorders that affect the interalveolar interstitium. ILDs are generally classified into idiopathic, autoimmune-related, exposure-related, interstitial lung diseases with cysts or airspace filling, sarcoidosis and orphan diseases [1]. Epidemiological studies have found major differences in the incidence of ILDs according to age, sex, ethnic origin and geographical region, which are caused by disparities in environmental exposure and inequalities in healthcare resources. A study published in 2022 estimated that the overall incidence (mean for six European countries) of ILDs ranged from 20.0 to 42.5 cases per 100,000 person-years, whereas the prevalence ranged from 33.6 to 247.4 per 100,000 person-years [2].

In the early stages of some ILDs, the accumulation of immune cells in the interstitium triggers inflammation. When this inflammation persists, aberrant scarring of the lesions can progressively replace the lung parenchyma, leading to pulmonary fibrosis (PF) and irreversible loss of lung function. Importantly, the inflammatory component of ILDs is reversible, whereas the fibrotic one is irreversible and can progress with rapid deterioration of the lung, as in the case of idiopathic pulmonary fibrosis (IPF) [3]. Fibrosing ILDs characterized by progressive and irreversible PF are defined as progressive PF (PPF) [4]. When known, the etiological agent that is responsible for the development of PF may be environmental, inflammatory or genetic. Some

---

Jean-Luc Desseyn and Valérie Gouyer contributed equally to this work.

✉ Jean-Luc Desseyn
jean-luc.desseyn@inserm.fr

[1] Univ. Lille, Inserm, CHU Lille, Infinite U1286, Lille F-59000, France

[2] Univ. Lille, Department of Pathology, CHU Lille, Lille F-59000, France

[3] Univ. Lille, CHU Lille, CNRS, Inserm, Institut Pasteur de Lille, UMR9020, UMR1277, Canther, Cancer Heterogeneity, Plasticity and Resistance to Therapies, Lille F-59000, France

[4] Univ. Lille, CNRS, Inserm, CHU Lille, Centre de référence constitutif des maladies pulmonaires rares, U1019, UMR 9017, CIIL, Center for Infection and Immunity of Lille, Lille F- 59000, France

environmental factors, such as tobacco smoke, occupational exposures, air pollution and viral infections, have been implicated in repeated damage to alveolar epithelial cells and stimulate the early processes of PF [5, 6]. Some patients with ILD associated with fibrosing autoimmune diseases, including rheumatoid arthritis or systemic sclerosis, develop a PPF phenotype [7]. Genetic variants are also associated with the risk of developing fibrotic ILDs [8, 9].

PF can be classified into distinct patterns according to morphological aspects. In particular, the usual interstitial pneumonia (UIP) pattern is associated with a poorer prognosis. UIP is preferably identified by high-resolution thoracic computed tomography. When possible, histological analyses of lung biopsies should be performed. In this case, fibrosis is subpleural and localized in the pulmonary periphery. Moreover, PF is temporally and spatially heterogeneous. Fibroblastic foci, which are characterized by the accumulation of fibroblasts/myofibroblasts and extensive fibrosis forming a honeycomb structure that is responsible for severe destruction of the lung architecture, are also observed [10, 11].

The mesenchymal component that produces connective tissue is critical for the repair of injured lung tissue. Fibroblasts have been identified as the major mesenchymal cell type in the connective tissue response, especially its activated form and its differentiated form as a myofibroblast, which is an important producer of extracellular matrix (ECM) and inflammatory and fibrogenic cytokines. The transformation of fibroblasts into myofibroblasts can be monitored based on the expression of mesenchymal cell markers, such as α-smooth muscle actin (α-SMA) [12]. Myofibroblast persistence at sites of injury leads to the formation of active zones of fibrosis, and lung epithelial damage and/or repair abnormalities trigger the recruitment of inflammatory cells into the lungs [13]. The combination of epithelial damage, abnormal wound healing and recruitment of inflammatory cells stimulates the synthesis of pro-fibrosing mediators, such as the transforming growth factor (TGF)-β1, interleukin (IL)-13 or the connective tissue growth factor thus promoting the differentiation of fibroblasts into myofibroblasts, which then actively proliferate and secrete excessive amounts of ECM, growth factors and metalloproteinases [14]. The accumulation of ECM degrades the epithelium, stimulates the recruitment of inflammatory cells and activates myofibroblasts, leading to a vicious cycle that magnifies fibrosis.

Currently, there is lack of satisfactory treatments for improving fibrotic ILDs. This is largely attributable to the lack of experimental models that can mimic the pathophysiological mechanisms of PF with progressive fibrosis. In this context, we report here a novel model of experimentally induced PF mimicking UIP features using mouse embryonic lung explants (MELEs) in an air/liquid interface (ALI) culture. Fibrosis was induced by a fibrosis cocktail consisting of a mixture of cytokines, a growth factor and an irritant, all of which have been described in the literature to be involved in the development of PF. This induced fibrosis was characterized, followed by the identification of genes that were upregulated and downregulated at the early stages of fibrosis.

Materials and methods

Organotypic culture of mouse embryonic lung explants

Reporter Acta2-Rfp (B6.FVB-Tg(Acta2-DsRed)1Rkl, RRID: IMSR_JAX:031159) transgenic mice that were bred hemizygously in-house at our institute and express DsRed RFP under the *αSMA* gene promoter (*Acta2*) and wild-type (WT) mice in the C57BL/6 genetic background aged between 2 and 6 months and between 2 and 8 months for females and males, respectively, were maintained and housed in an accredited specific pathogen-free animal facility. The mice were fed with a chow diet *ad libitum*. MELEs were harvested under a stereomicroscope (as described by Del Moral and Warburton [15] from 12.5-day-old embryos (E12.5) and placed on a porous polycarbonate filter (1000M25/511M801, it4ip, Belgium) that was floated in 4-well plates containing 500µL of serum-free DMEM/F12 with antibiotics (penicillin and streptomycin). The MELEs were then cultured in ALI at 37 °C with 5% CO_2. MELE growth and Rfp fluorescence were monitored daily under a Leica M205 FA LasX epifluorescence stereomicroscope equipped with a 16-bit Hamamatsu camera (sCMOS ORCA-Flash4.0) at 30 magnification. Images of MELEs were captured every day from day 0 (day of dissection) to the last day of culture. Images were acquired at an exposure of 100ms for bright field and 1s for Acta2-Rfp fluorescence. The fluorescence intensity was quantified using FIJI freeware (RRID: SCR_002285) and was normalized to the surface area of the MELE.

Induction of fibrosis by fibrotic cocktail

The design of the fibrotic cocktail (FC) used here was adapted from the literature [16–18] and comprised cytokines (Merck, Darmstadt, Germany) TGF-β1, platelet-derived growth factor (PDGF)-AB, IL-1β, IL-13 and tumour necrosis factor (TNF)-α as well as lysophosphatidic acid (LPA, Cayman Chemical) and cadmium chloride ($CdCl_2$, Merck, Darmstadt, Germany), an irritant factor. Final concentrations were 10ng/mL TGF-β1, 10µM PDGF-AB, 20ng/mL

TNF-α, 10μM LPA, 20ng/mL IL-1β, 20ng/mL IL-13 and 4μM $CdCl_2$. FC or phosphate-buffered saline (PBS; as a control) was administered daily from day 2 of MELE culture to a maximum of 4 days of culture in 300μL of serum-free DMEM/F12 with antibiotics. Once the MELE culture was stopped, the MELEs were fixed with 4% paraformaldehyde for 18 h, then embedded in paraffin for histological and immunohistochemistry studies. Tissues that were collected for RT-qPCR were placed directly in RNAlater (Sigma-Aldrich) for 24 h at 4 °C, then stored at −80 °C until use.

Quantification of RFP

The Acta2-Rfp-positive areas were quantified and normalized with respect to the whole tissue area for each sample. For each day of MELE culture, the change in Acta2-Rfp production is given as a percentage change compared to day 0.

Histology and immunofluorescence

Haematoxylin/eosin (HE), Sirius Red (SR) and Masson Trichrome (MT) histological staining of MELE sections, as well as immunohistochemical assays were performed as described previously [19, 20] using dual labelling for anti-α-Sma (Abcam ab7817, RRID: AB_262054) and anti-vimentin (Abcam ab137321, RRID: AB_2921312) antibodies. Subsequently, staining with secondary antibodies (Jackson ImmunoResearch labs; rhodamine-conjugated anti-mouse 315-026-00, RRID: AB_23400583 and fluorescein-conjugated anti-rabbit 111-095-047, RRID: AB_2337977 antibodies) was carried out. The sections were observed under a Leica DM5500B epifluorescence microscope and analysed using the FIJI freeware.

Histopathological evaluation of lung fibrosis

Fibrosis on HE and SR histological sections was scored blindly by two team members. The obtained score was the sum of the Ashcroft score [21], which ranges from 0 to 8, and a peripheral PF score ranging from 0 (no fibrosis) to 3, as follows: 0, no area of fibrosis; 1, area of fibrosis accounting for 0–20%; 2, area of fibrosis accounting for 20–40%; 3, area of fibrosis accounting for >40% of the area that was assessed. The severity of the fibrotic changes in each section was assessed as the mean score of the severity on sections from 10 MELEs treated with PBS and 12 MELEs treated with FC after 3 days of culture; 11 MELEs treated with PBS and 14 MELEs treated with FC after 4 days of culture; and 12 MELEs treated with PBS and 15 MELEs treated with FC after 5 days of culture. The pattern of PF was determined by an expert pathologist in human ILDs from the Lille University Hospital Reference Centre for Rare Pulmonary Diseases (SH). Macros for ImageJ/FIJI were used to quantify fibrosis and airspace in whole slices stained with SR as described by others [22].

Quantitative real-time RT-PCR

Total RNA extraction was performed on MELEs using an innuPREP RNA Mini Kit 2.0 (Innuscreen GmbH, Germany), and reverse transcription was carried out as described previously [23]. Duplex PCR amplifications using 18S rRNA as an internal control (TaqMan Ribosomal RNA Control Reagents, Applied Biosystems) were performed as described previously [24]. Semi-quantitative PCR for the detection of specific genes was performed using the following primer set and probe (5’→3’) designed using Primer3 (RRID: SCR_003139): mouse *Tgf-β1* (ENSMUSG00000002603), AGGAGACGGAATACAGGGCT (Fwd), TCATGTCATG GATGGTGCCC (Rev) and GCGCTCACTGCTCTTGTG ACAGCA (probe); *Col1a1* (ENSMUSG00000001506), CT GCTGGCTCTCCTGGTAC (Fwd), GAAGACCAGGGAA GCCTCTT (Rev) and ACGTGGTGTGGTCGGTCTTCCC (probe); *Acta2* (ENSMUSG00000035783), TCCCTGGAG AAGAGCTACGA (Fwd), CCGCTGACTCCATCCCAAT G (Rev) and ACGAACGCTTCCGCTGCCCA (probe). To avoid the amplification of contaminating genomic DNA, the primers and/or the probes were designed on different exons or overlapping exon−exon junctions. Amplifications were performed in triplicate on a 7500 Applied System (Applied Biosystems). For each sample, the ratio of amplification was calculated as $2^{-(\text{Ctmean target gene} - \text{Ctmean 18S})}$.

Single-cell RNA-sequencing 3′ (10× genomics)

WT MELEs were treated at day 3 of culture for 18 h with either PBS (*n*=6) or FC (*n*=6). The trachea was then removed under a stereomicroscope using microdissection forceps. Six MELEs per group were then pooled. Cell dissociation was performed in DMEM/F12 containing 5% liberase (05989132001, Roche, Germany), 1% DNase I (09852093103, Roche, Germany) and 5% foetal bovine serum (FBS, 10270106, Thermo Fisher Scientific) for 2 h at 37 °C. During this step, mechanical dissociation of MELEs was performed every 15 min using a large orifice tip. Ten minutes before the end of the reaction, 0.05% trypsin EDTA was added to each pool. Dissociation was stopped by adding 2 volumes of 10% FBS. A final mechanical dissociation using large-orifice tips was performed. To remove cell aggregates, the cells were filtered through a 70 μm filter and then centrifuged for 15 min at 1400 rpm. Dead cells were removed using a Dead Cell Removal kit according to the manufacturer's instructions (Miltenyi Biotech, Germany). Cells were then pelleted by centrifugation for 10 min at 1400 rpm and the pellets were resuspended in 100µL of PBS containing 0.04% bovine serum albumin (BSA). Cells were counted on a Malassez counting chamber and diluted to 800 cells/µL in PBS containing 0.04% BSA. A single-cell RNA-sequencing 3′ (scRNAseq3′) analysis was performed using the Chromium Next GEM Single Cell 3′ Kit (10x genomics, v3.1) technology at our genomics core facility. Sequencing was calibrated on the *Mus musculus* organism using an Illumina NovaSeq 6000 sequencer. The primary analysis after sequencing was performed using the Cell Ranger tool (version 5.0, RRID: SCR_017344). For quality control, we used the scDblFinder tool (RRID: SCR_022700) [25] exclude cells expressing more than 7716 or less than 200 genes, cells potentially undergoing apoptosis with $>10\%$ mitochondria and cell doublets. Bioinformatics data were then analysed using the R freeware environment (RRID: SCR_001905) and the Seurat package (RRID: SCR_007322). Sequencing data from cells treated with PBS or FC were merged to retain only the genes in common. The measured genes were normalized using NormalizeData (LogNormalize method) and a scale factor of 10,000. Data were transformed using the Seurat scale.data tool. A principal component analysis was then performed. The ElbowPlot method identified 30 principal components. A resolution of 0.8 was applied via the shared nearest-neighbour function from the first 30 principal components to design uniform manifold approximation and projection (UMAP) maps of cell clusters. Cell types were assigned to clusters using the source file https://github.com/IanevskiAleksandr/sc-type [26]. The ggplot2 function of R (RRID: SCR_014601) was used to design the figures, and the plotly tool (RRID: SCR_013991) was employed to generate the interactive links. The ToppFun tool from the Toppgene website (RRID: SCR_005726) was used to identify the various biological processes that were associated with under- or overexpressed genes. The STRING website (RRID: SCR_005223) was used to model the interactions between the proteins expressed from genes that were overexpressed in the FC condition. The GOrilla (RRID: SCR_006848) website was used for gene ontology analysis. The original datasets of scRNAseq3′, analysis R scripts and code for the interactive 3D representations of the UMAP superposition have been deposited in a free and open digital archive, Zenodo (RRID: SCR_004129), which is available at https://doi.org/10.5281/zenodo.13285840.

Statistical analysis

Nonparametric tests were performed for all statistical analyses using the R software environment, version 3.6.3. Wilcoxon-Mann-Whitney two-sided test and Kruskal-Wallis test were used for analysis as appropriate for all experiments, with the exception of the analysis presented in Fig. 5C, in which a two-sided two-proportion Z-test was performed. The volcano plot was established with a *P*-value limit adjusted to 0.05% and a log2-fold change cut-off of −2.0/2.0. Significance was set at $P<0.05$.

Results

Set up of the optimal parameters for the induced fibrosis model

Pilot studies were first carried out to determine the best FC for the induction of fibrosis in our MELE model in an ALI culture. The selected compounds and their concentrations were as described in the literature. These studies enabled us to select the FC that induced the greatest PF according to the results obtained after the histological and immunofluorescence analyses (not shown).

Next, we measured its pro-fibrotic effect on the development of fibrosis in embryonic lungs using the *Acta2-Rfp* reporter transgene driven by the *α-SMA* promoter, according to the experimental scheme displayed in Fig. 1a. Explant areas increased daily with no significant difference for each day between the two conditions tested, i.e. PBS vs. FC (Suppl. Figure 1). The myofibroblast reporter allowed the daily semi-quantification of each MELE using stereomicroscopy. Repeated administration of the FC altered the apparent structure of the MELEs, which became increasingly dense in white light, with thickening of the lung parenchyma (Fig. 1b). These morphological changes were associated with a significant overall increase in the expression of the *Acta2-Rfp* reporter gene in FC-treated MELEs (Fig. 1c).

Characterization of the induced fibrosis

We then examined the induction of fibrosis. All the following results were obtained using the experimental scheme mentioned as above (Fig. 1a), with the exception of the used of WT mice exclusively for mating, to avoid the introduction of any possible bias by the *Acta2-Rfp* transgene. Histological analysis via HE and SR staining revealed the progressive appearance of structural changes, signs of fibrosis and fibroblastic foci, which were visible at day 4 after 2 days of treatment. Numerous collapsed alveoli were observed in FC-treated MELEs, accompanied by the thickening of the alveolar septa. An accumulation of ECM, as reflected by SR staining, in bundle form, and the presence of interstitial fusiform cells in the basal and subpleural regions were also detected, as illustrated in Fig. 2a, and were and confirmed

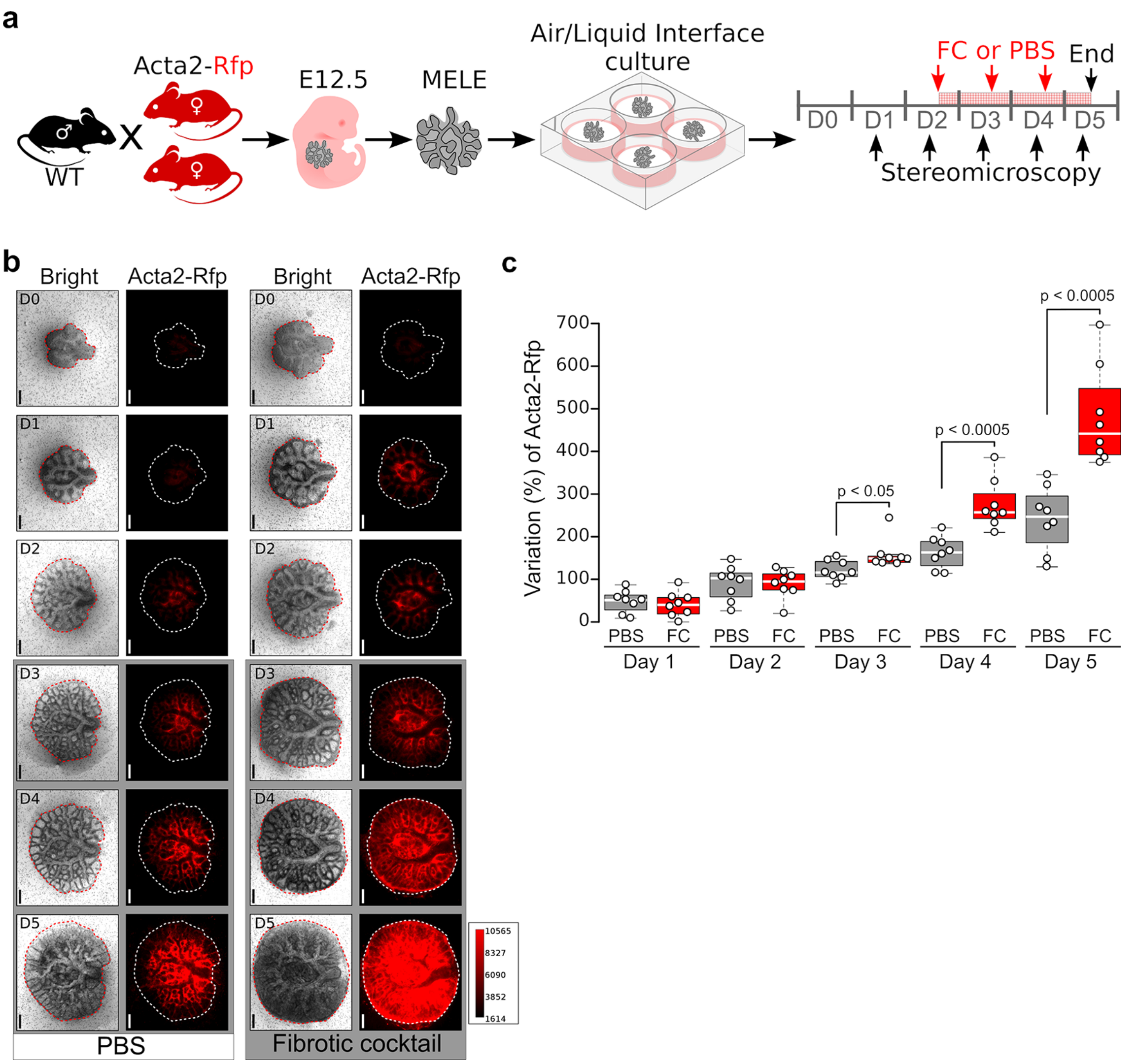

Fig. 1 The fibrotic cocktail enhanced the expression of the *Acta2* reporter transgene. (**a**) Schematic representation of the protocol used here for obtaining and culturing mouse embryonic lung explants (MELEs). After 2 days (D) of culture, PBS or the fibrotic cocktail (FC) was added to the culture medium. MELEs were observed daily under white light and epifluorescence for the Rfp transgene reporter tag. (**b**) Images at 5 days of culture of representative MELEs treated with PBS or FC, showing an increase in their density (bright light) and a thickening of the lung parenchyma. Scale bar: 500 µm. (**c**) Quantification of the variation in the fluorescence intensity emitted by Acta2-Rfp from the total surface of MELEs ($n=8$/group), from day 1 to day 5

using MT staining (Suppl. Figure 2). These more-marked abnormalities in FC-treated MELEs are characteristic of fibrosis, which was found to be heterogeneous. All of these histological features are present in the UIP pattern. Next, we assessed the fibrosis using our fibrosis scale, to quantify the severity of fibrosis considering the extent of fibrosis in the lung periphery from day 3 to day 5 of treatment. Our results revealed that the fibrosis scores were significantly higher for FC-treated MELEs, with an increase in fibrosis observed daily (Fig. 2b). This was further supported by the quantification of the induced-fibrosis using SR staining sections after removing the trachea for the analysis showing a significant increase in fibrosis over time, and this only in CF-treated MELEs (Fig. 2c,d).

The expression of genes associated with inflammation (*Tgf-β1*, Fig. 3a) and fibrosis (*Col1a1* and *Acta2*, Fig. 3b,c) was assessed by RT-qPCR. No difference between the two treatments was observed at days 3 and 4 for *Tgf-β1*, whereas its expression level was higher at day 5 in FC-treated MELEs. The expression levels of *Col1a1* and *Acta2* showed a trend toward upregulation at day 3 in FC-treated MELEs, and significant upregulation at day 4 and at days 4 and 5, respectively. We then used immunofluorescence staining to examine the production and localization of α-Sma and vimentin (the latter being a component of the intermediate filaments of cells of mesenchymal origin, including fibroblasts and myofibroblasts) (Fig. 4, Suppl. Figure 3c, d). We observed a progressive accumulation of the two

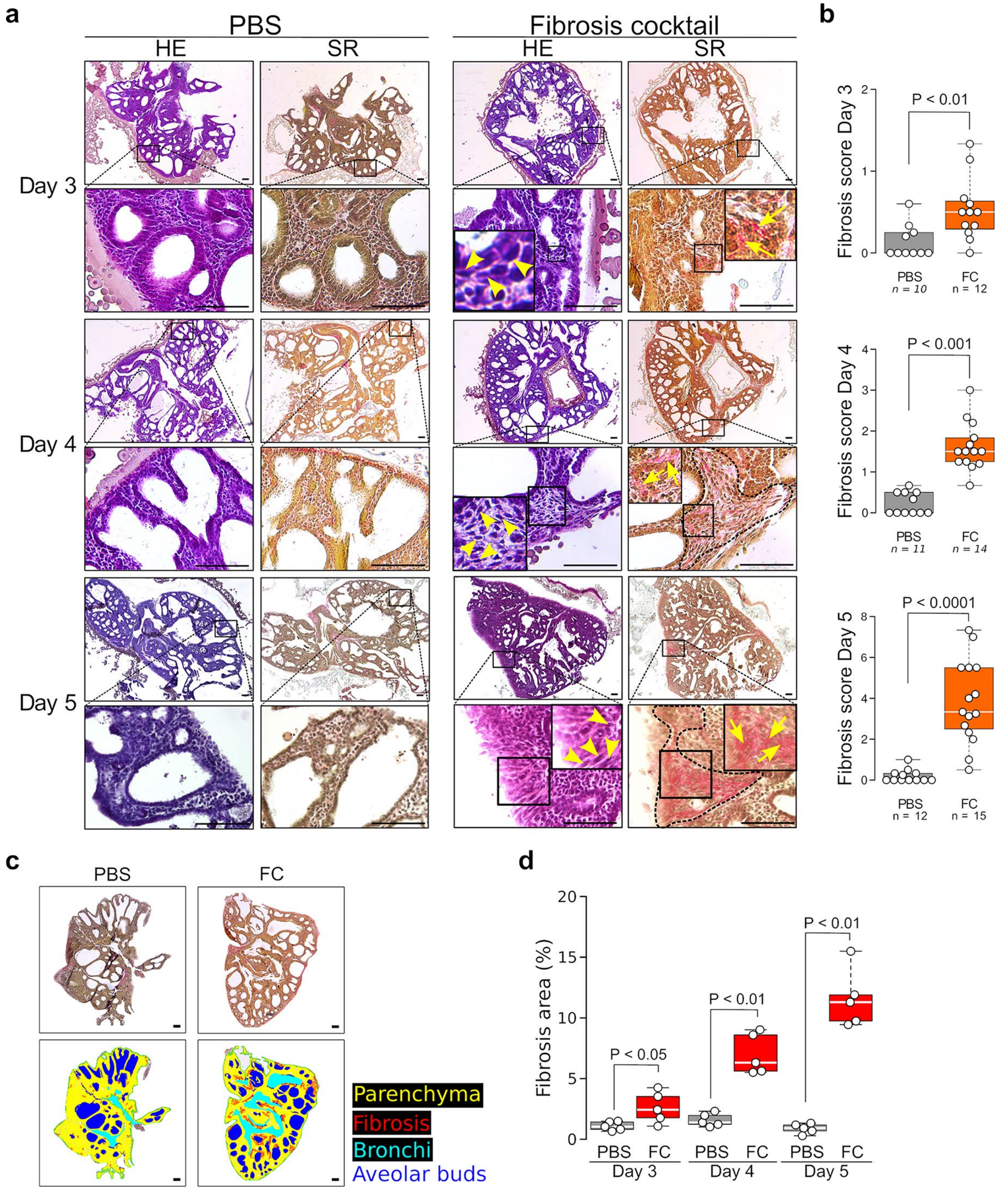

Fig. 2 Histological analysis revealing induced fibrosis in the lung periphery, similar to a UIP pattern. (**a**) Illustrative images of haematoxylin/eosin (HE)- and Sirius Red (SR)-stained sections at days 3–5 from mouse embryonic lung explants (MELEs) treated with PBS or the fibrotic cocktail (FC), indicating a reduction in the alveolar bud lumen and a progressive and peripheral accumulation of spindle cells associated with collagen densification. The yellow arrowheads indicate spindle cells. The yellow arrows denote collagen fibre deposits. The area surrounded by black dotted lines indicates fibroblastic foci with dense regions of collagen. The images are representative of 10–15 MELEs/day/group. Scale bar: 100 µm. (**b**) Severity of fibrosis after FC administration, as evaluated using a modified Ashcroft scale. Data were obtained from *n* = 10–15 MELEs/group. (**c**) Illustrative pictures of the follow-up of collagen accumulation on MELE sections in SR staining at day 4 of culture. A plug-in for ImageJ/FIJI software automatically identified lung parenchyma (yellow), fibrosis (red) and alveolar buds (blue). Bronchi (cyan) were traced by the user. Scale: 100 µm. (**d**) Graph showing the fibrosis area (%) for each MELE depending of the type of treatment and the day on which culture was stopped. *N* = 5/treatment/day. *P*-value from the Kruskal-Wallis test was *P* = 0.002 for FC in (**d**) and not significant for the PBS group

Fig. 3 *Tgf-β1* (**a**), *Col1a1* (**b**) and *Acta2* (**c**) mRNA quantification in mouse embryonic lung explants treated with PBS or the fibrotic cocktail (FC) was performed using RT-qPCR in triplicate ($n = 7$–8 explants/group)

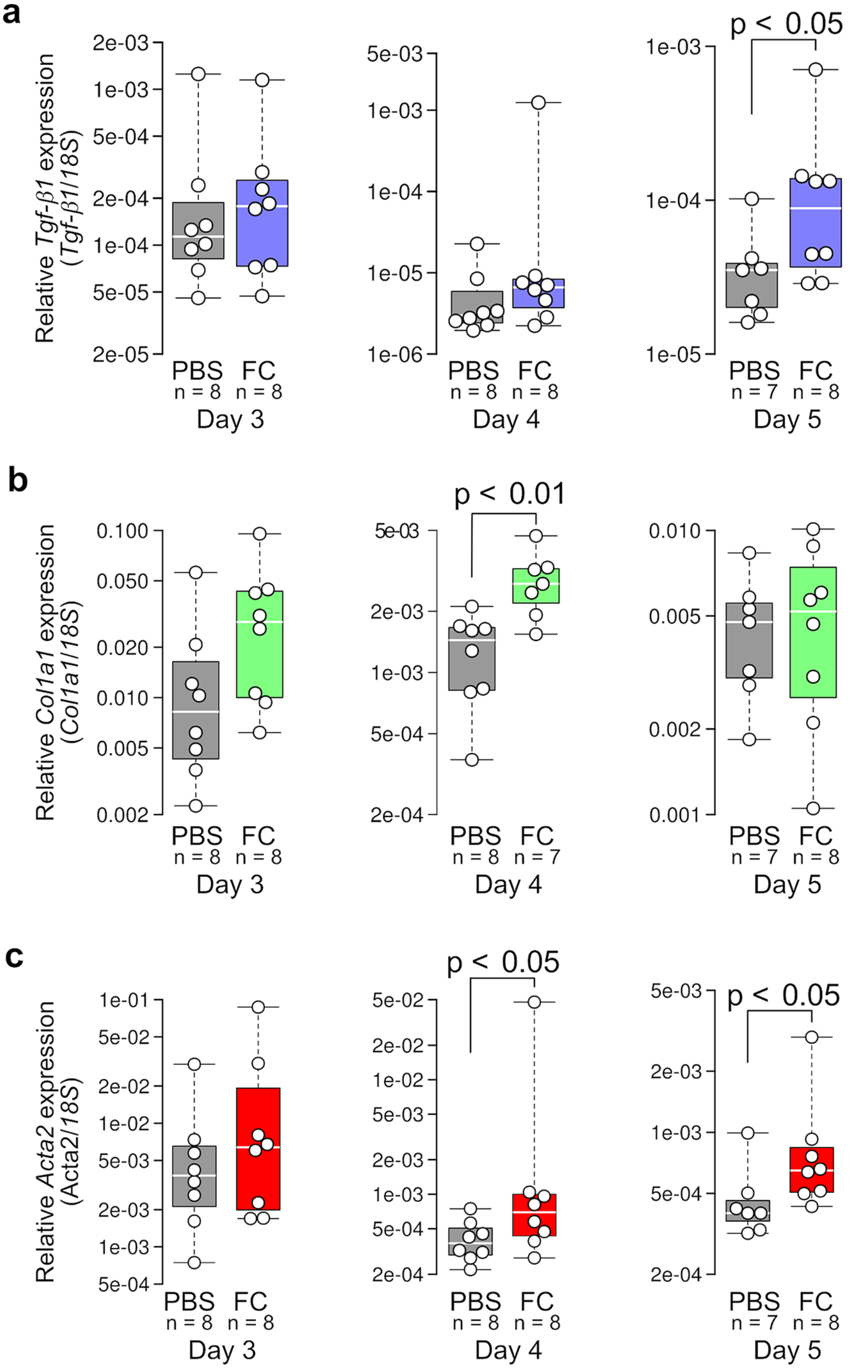

biomarkers of fibrosis in the lung periphery in FC-treated MELEs, reflecting the increased proliferation and activity of peripheral myofibroblasts. Taken together, these data demonstrated that the repeated administration of FC stimulated the proliferation and activity of myofibroblasts in the pulmonary periphery, leading to the overexpression of markers of inflammation and fibrosis.

Early modifications of gene expression

Next, we used our new PF model to determine the pattern of the early changes in gene expression via scRNAseq3′, to identify target candidate genes in lung fibrosis. For this purpose, cells were isolated after a mere 18 h of treatment with either PBS or our FC. Analyses were performed by comparing two pools corresponding to the two treatments, each comprising six treated MELEs (Fig. 5a). All data were analysed using 12,893 and 8,471 curated cells for the PBS

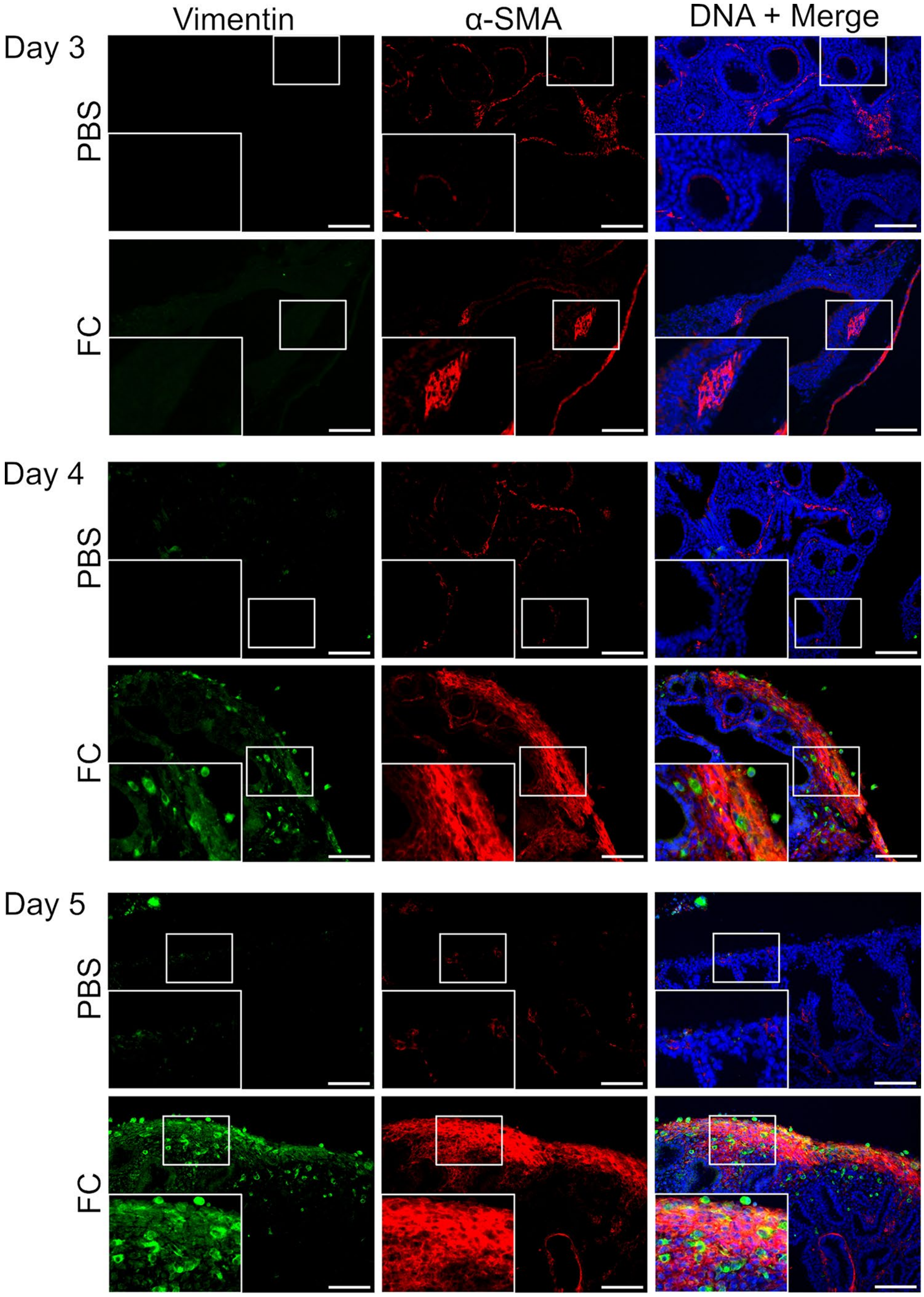

Fig. 4 Immunofluorescence analysis of parenchyma from PBS (control)- and fibrotic cocktail (FC)-treated lung explants at days 3–5. Immunofluorescence staining for vimentin (green) and α-Sma (red) showing the progressive accumulation of mesenchymal cells and fibrosis labelled by α-Sma in the lung periphery of the mouse embryonic lung explants. Nuclei are counterstained with the Hoechst 33,258 dye (blue). Scale bar: 100 µm

and FC-treated MELEs, respectively. The assignment of cell types to clusters was based on a source file of assigned human data. Therefore, we decided to carry out a preliminary compatibility check between human and mouse embryonic lung genes, to limit any interpretation biases, using the reference atlas of mouse embryonic lung development published in 2021 [27]. Using cell-type gene signatures, we identified 12 major cell types. UMAPs from the differentially expressed gene analysis between clusters to outline cell subsets with unique molecular signatures, revealed the presence of not only overlaps between the two groups, but also enriched cell clusters (Fig. 5b, Suppl. Figure 4a). Interactive 3D representations of the UMAP superposition for the two conditions, without or with cell clustering, are available at the following URLs: https://cbedart.github.io/scRNAseq/Hennion2024/UMAP_Conditions/ and https://cbedart.github.io/scRNAseq/Hennion2024/UMAP_Celltypes/, respectively. A 3D UMAP representation grouping both conditions and cell types is available at the following URL: https://cbedart.github.io/scRNAseq/Hennion2024/UMAP_Celltypes_Conditions/. Comparison of the two conditions revealed a very high number of myofibroblasts in the FC

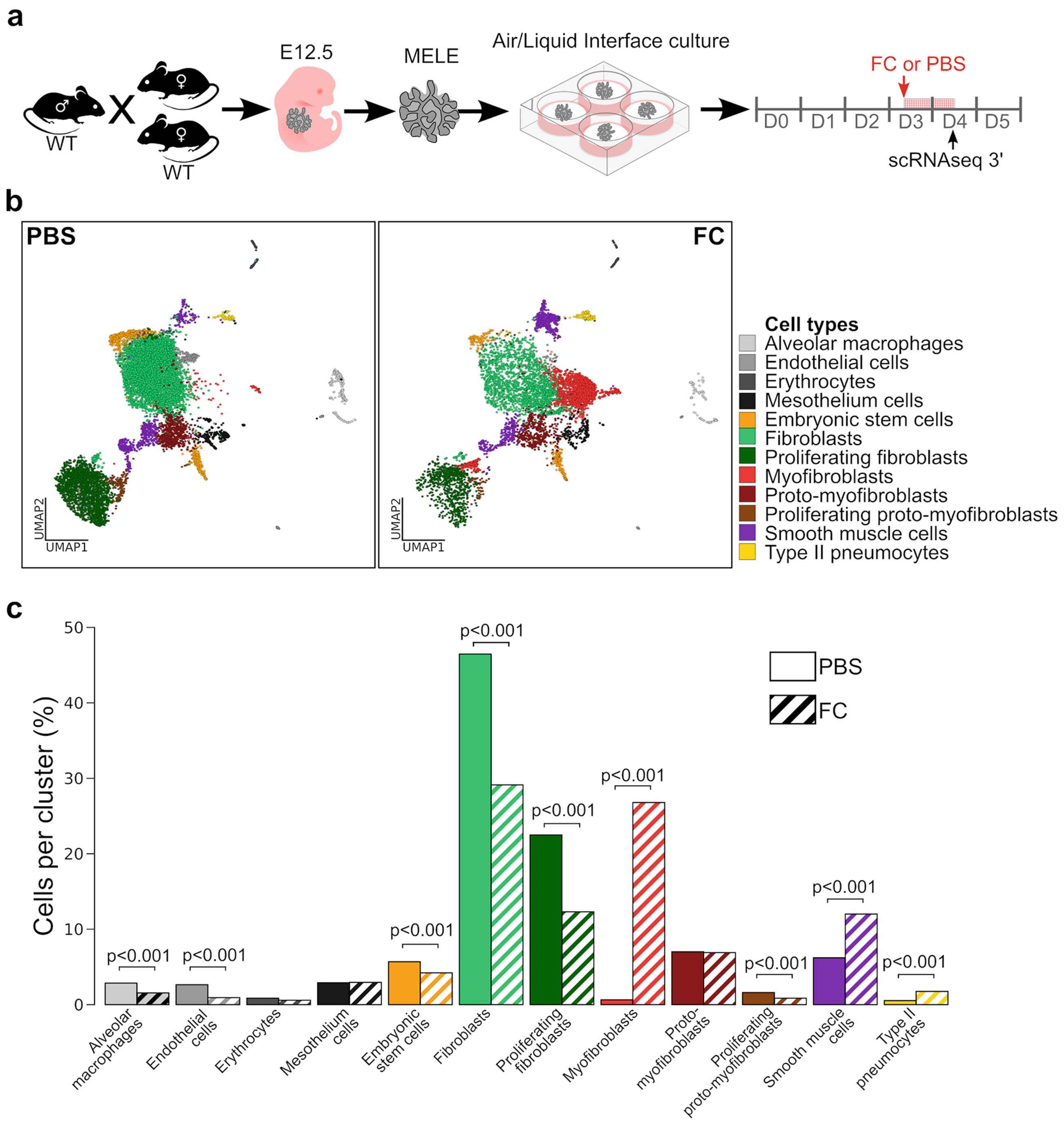

Fig. 5 Single-cell RNA-sequencing 3′ analysis of early fibrosis. (**a**) Schematic representation of the protocol used here for the scRNAseq3′ analysis of mouse embryonic lung explants (MELEs). MELEs were treated with PBS or the fibrotic cocktail (FC) from day 3 of culture, then analysed the following day. WT = wild type. (**b**) Dimensional reduction of data generated from control (PBS)- and fibrotic cocktail (FC)-treated mouse embryonic lung explants (MELEs), as visualized by uniform manifold approximation and projection (UMAP), with each distinct cell type defined by a specific colour (as indicated in the key). (**c**) Bar charts of the relative abundance (%) of each cell type in the control (PBS)- and FC-treated MELEs. Significant *P*-values (Z-test) are indicated

condition (26.8%) compared with the PBS control (0.7%) and a 2-fold higher relative proportion of smooth muscle cells (12% for FC vs. 6.2% for PBS). This was accompanied by a 2-fold higher proportion of fibroblasts in the PBS condition (46.4%) compared with the FC condition (29.1%), and of proliferating fibroblasts (22.5% and 12.3% for PBS and FC, respectively) (Fig. 5c, Suppl. Figure 4b).

The scRNAseq3′ analysis allowed the comparison of gene expression profiles in an unbiased manner between PBS-treated control MELEs and the FC-treated MELEs.

This analysis revealed that 25 genes were downregulated and 112 genes were upregulated in cells from FC-treated MELEs (Fig. 6a, Suppl. Tables 1 and 2). The corresponding interactive volcano plot can be accessed via URL: https://cbedart.github.io/scRNAseq/Hennion2024/VolcanoPlot/. Most of the overexpressed genes detected here were known to be involved in the inflammatory response. Genes linked to the acute inflammatory response, such as *Saa1*, *Hp* or *Cp*, or to chronic inflammation, such as *Cxcl13*, *Cxcl1* and *Ccl11*, were overexpressed in the fibrosis-induced condition. In a concomitant response to inflammation, genes encoding ECM proteins, such as *Col18a1*, *Col22a1* and *Postn*, were overexpressed (suggesting early activation of genes involved in fibrosis), as were wound-healing genes, such as *Ccl2* and *Mmp9* (Fig. 6b). A broader analysis of gene expression illustrated by the Heatmap using the 50 most differentially expressed genes, based on adjusted *P*-values and Log2 fold changes, highlighted many genes that are involved in inflammation and fibrosis. In addition, although these genes were overexpressed in all cell types, they were over-represented in the myofibroblasts of FC-treated MELEs (Fig. 6c). The *Ccl2*, *Cxcl1*, *Ccl7* and *Cxcl5* inflammatory genes were overexpressed in mesothelial and mesenchymal cells, with myofibroblasts predominating in the FC condition (Fig. 7a). The identification of interactions of the proteins encoded by the genes that were overexpressed after FC treatment revealed numerous inflammatory mediators that interacted with each other. Most of these inflammatory proteins were part of the acute phase of inflammation, including Saa- and Serpina-family proteins. Moreover, numerous cytokines and mediators of the complement system linked to inflammation interacted with each other (Fig. 7b). In addition to inflammation-associated genes, genes related to fibrosis were also upregulated in MELEs with induced fibrosis (Fig. 8a). The *Postn*, *Col18a1* and *Ccn1* fibrosis genes were upregulated in myofibroblasts, with *Ccn1* also being upregulated in type II pneumocytes and endothelial cells. To gain further insights into the set of genes that were upregulated in the induced vs. not-induced fibrosis conditions, we performed a GOrilla gene ontology analysis (Fig. 8b). This revealed a pathway associated with metal and ion homeostasis, as indicated by the upregulation of genes encoding Mt2, Steap4, Cp, Lcn2 and Sod2 (Fig. 8c).

Discussion

PF affects a considerable number of individuals worldwide. To identify therapeutic solutions for this condition, a wide variety of pre-clinical models have been developed. However, the current treatment strategies remain unsatisfactory in many cases, likely because no experimental model can accurately recapitulate the pathophysiological mechanisms of human PF [28]. Therefore, we developed a novel model based on the experimental induction of PF in MELEs. This mammalian model can be considered as being “integrated”, albeit incomplete, as it is embryonic; nevertheless, it has the advantage of being able to allow transcriptomics analyses without a priori studies by scRNAseq3′ of the whole lung, as illustrated by the present study. This approach avoids the majority of the immune component and the host response to microbial colonization of the lung tissue, which pollute the transcriptome. This is crucial for gaining a more comprehensive understanding of gene expression within lung cells. Another advantage of this model is the relative ease with which the development of fibrosis can be monitored daily using microscopy of the whole organ, with detection of morphological and expression changes in fibrosis biomarkers being performed using genetically modified reporter mice for these markers. Finally, the use of a whole organ in culture should guarantee reproducible and heterogeneous fibrosis between explants compared with fibrosis induced on whole animals.

A plethora of experimental protocols for inducing PF have been published to date. Among them, intratracheal instillation of bleomycin into mice remains the most widely used approach, albeit with limitations, as it induces histopathological patterns that are not sufficiently consistent with those identified in patients with PF [29, 30]. Therefore, we relied on the use of a cocktail to induce fibrosis in our explant model. Its composition was adapted from literature data [16–18]. Our preliminary studies suggested, according to the Acta2-RFP reporter, that the cytokine concentrations often used by others (10ng/mL) on primary cell cultures, higher than the physiological concentrations found in patients with pulmonary fibrosis [31], did not seem satisfactory in contrast to our results by doubling the concentrations. Because cadmium is a recognized cause of lung fibrosis in humans, we also added this heavy metal at 4µM, i.e. at twice the concentration found in smokers [17]. The agents used here were all known to be upregulated and involved in the pathophysiology of PF by promoting, among other events, the proliferation and differentiation of fibroblasts into myofibroblasts, the overexpression of α-SMA and the overproduction of ECM [32–34]. In our model, induced fibrosis progressed well and was characterized by the presence of spindle cells and dense collagen fibres in basal and subpleural regions. These features were very similar to those of subpleural interstitial fibrosis, which is characterized by the accumulation of fibroblasts/myofibroblasts forming fibroblastic foci that is typically observed in histopathological analyses of patients with the UIP pattern [35]. The expression of fibrosis biomarker genes, such as *Acta2* and *Col1a1*, was clearly upregulated, accompanied

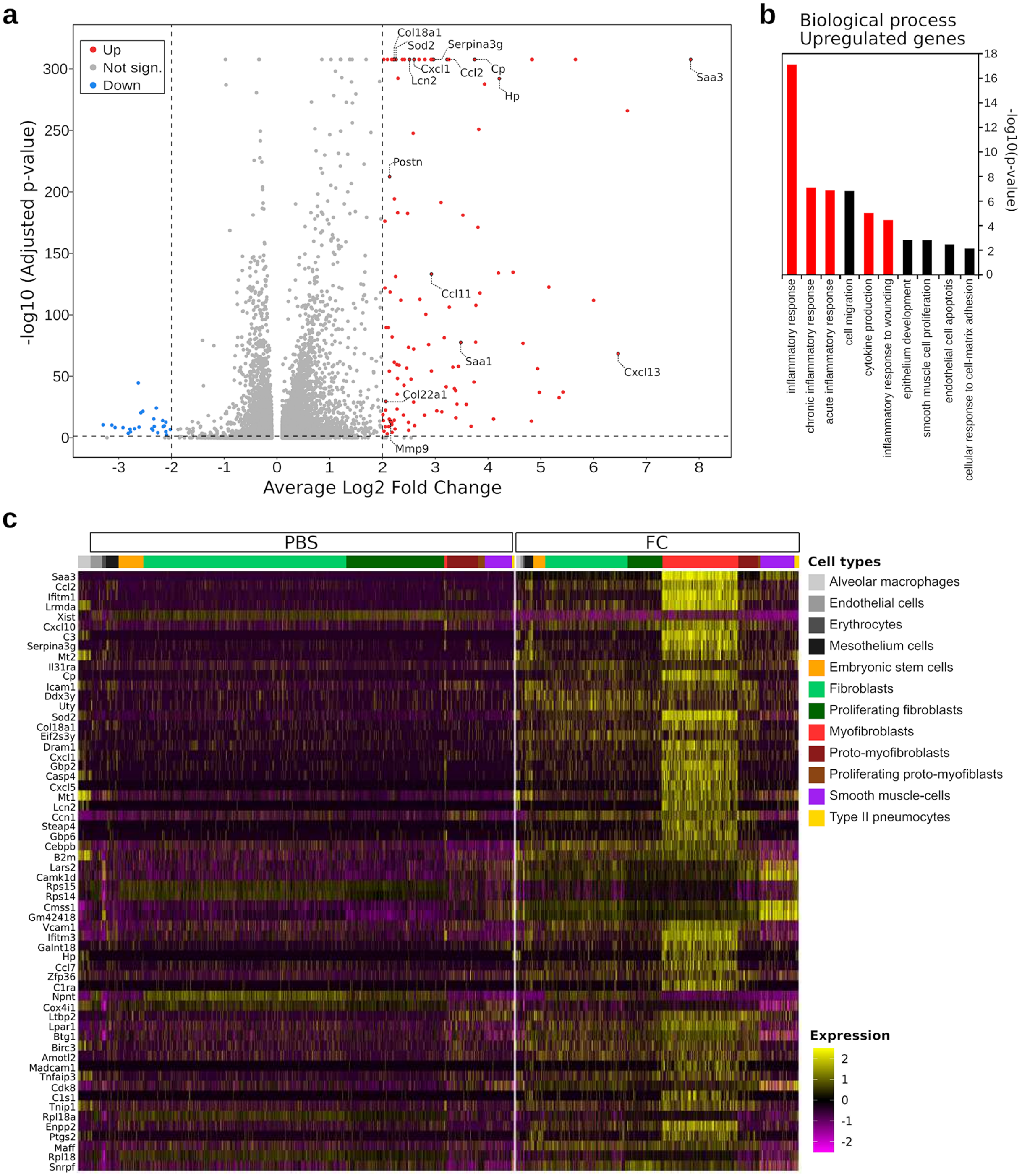

Fig. 6 The fibrotic cocktail upregulated genes involved in inflammation. (**a**) Volcano plot showing adjusted *P*-values and log2 fold change of expression in all cell clusters. The blue dots ($n=25$) correspond to downregulated genes, the red dots ($n=112$) correspond to upregulated genes and the grey dots ($n=11{,}766$) indicate an absence of significant differences compared with the control condition. The adjusted *P*-value cut-off was set at 0.05, and the log2-fold change mean cut-offs were set at −2 and 2. (**b**) Biological processes identified for the genes that were overexpressed after treatment with the fibrotic cocktail (FC), as assessed based on the ToppFun tool from the ToppGene Suite. The red bars indicate biological processes involved in inflammation. (**c**) Heat map visualizing the expression of the 50 most differentially expressed genes according to cell type after treatment with FC compared with the PBS control

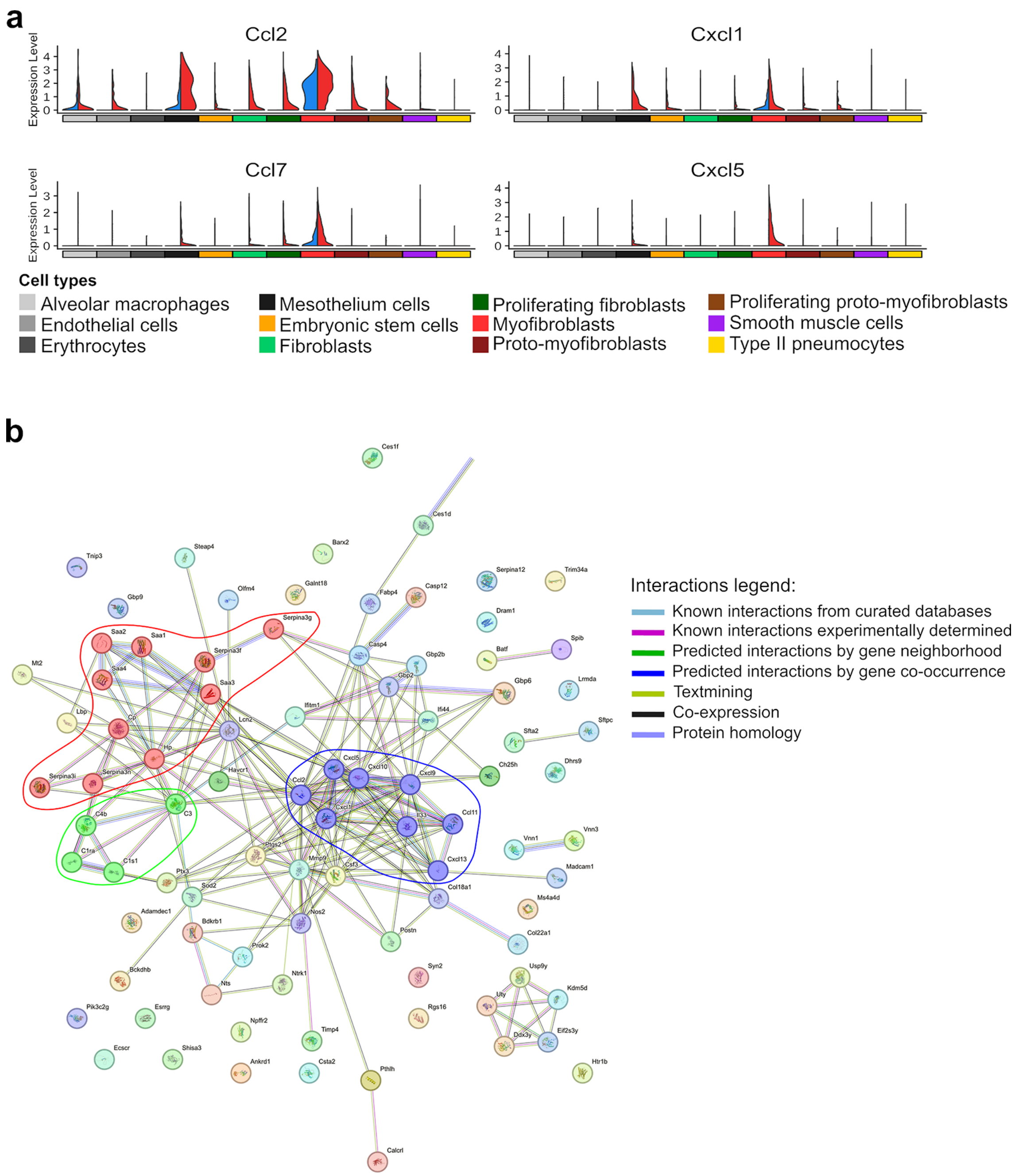

Fig. 7 Upregulation of genes associated with inflammation. (**a**) Violin plots showing the overexpression of genes associated with inflammation in mouse embryonic lung explants treated with the fibrotic cocktail (red) compared with the PBS-treated controls (blue). Cell types are indicated by specific colours, as shown in the key. (**b**) Protein interaction network based on the genes that were overexpressed in lungs with induced fibrosis. The three families of proteins associated with inflammation are circled in red, green or blue for mediators of the acute phase of inflammation, complement system proteins and cytokines, respectively. The results were obtained using the STRING application

by significant accumulation of fibrosis markers (α-Sma) and mesenchymal cell markers (vimentin). Remarkably, these same markers have been found to be upregulated in patients with IPF and in some experimental models of PF [36, 37]. Obviously, the nature, frequency, kinetics and concentrations of the molecules included in our cocktail remain empirical, and other compounds and experimental conditions warrant tested in the future.

As described above, FC administration to the MELE model induced a heterogeneous PF that was marked by subpleural invasion of fibroblasts and myofibroblasts, forming fibroblastic foci that triggered ECM production and accumulation. This is a typical feature of the UIP pattern, and

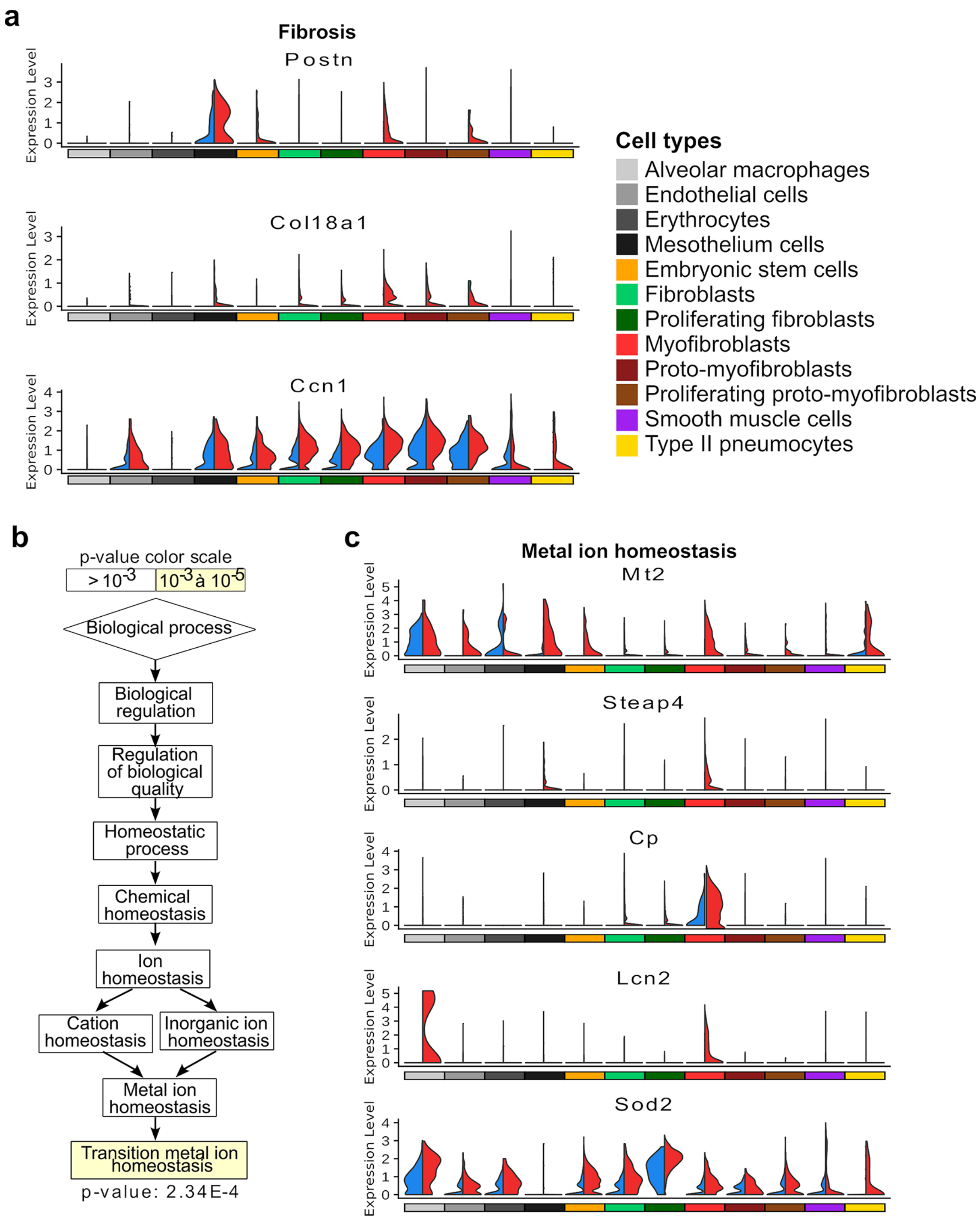

Fig. 8 Genes associated with fibrosis and metal ion homeostasis after treatment with the fibrotic cocktail. (**a**) Violin plots revealing the overexpression of genes associated with fibrosis in mouse embryonic lung explants (MELEs) treated with the fibrotic cocktail (red) compared with control MELEs treated with PBS (blue). (**b**) Graph of the biological process by the GOrilla analysis outlining metal ion homeostasis in the process of induced pulmonary fibrosis. (**c**) Violin plots reveal overexpression of genes linked to metal ion homeostasis for MELEs with induced fibrosis (red) compared to PBS-treated controls (blue)

few experimental models are capable of reproducing it. However, the UIP pattern is characterized by the formation of a honeycomb structure, which is a sign of advanced-stage PF; we did not observe this type of structure in our model. This can be explained by the fact that our model mimics an early stage of PF, before the potential formation of the honeycomb structure. More specifically, our model is similar to a probable UIP [38].

As our model developed a fibrotic profile of interest after several days of induction, we conducted a transcriptomics study using single-cell RNA-sequencing after a mere 18 h of induction, i.e., before histological signs were visible, to identify a very early signature of induced fibrosis. This transcriptomics study highlighted the quantitative differences in the nature of cell types between lungs without induced fibrosis and lungs with induced fibrosis, with a significant increase in the number of myofibroblasts, which are key cells in the development of fibrosis, smooth muscle cells and type II pneumocytes, as well as a relative decrease in the number of endothelial cells. These results are perfectly in agreement with the observations reported for several models of experimental PF [39–41].

The early genetic signature of our model remained closely linked to inflammation and fibrosis, whereas the phenotypic manifestations of fibrosis were not yet visible. The expression levels of the genes identified here were similar to those found in other atlases derived from lung tissue from mouse models with induced PF or from patients with ILD. In fact, the upregulation of the *Lcn2*, *Serpina3g* and *Cp* observed here was also present in the Curras-Alonso atlas, which is based on a mouse model of PF induced by radiation [42]. Regarding the expression of *Ccl2*, *Postn* and *Col18a1* in our analysis, they are overexpressed in the ILD atlas [43]. These data support the interest and relevance of our induced fibrosis model.

Several gene families that were upregulated in the pro-fibrotic condition have been well documented as being involved in the pathophysiology of PF. Among the gene families identified in our model, we found inflammation-related genes encoding proteins that are involved in the acute phase of inflammation, such as the serum amyloid A (SAA) family. In fact, the serum SAA levels are higher in patients with IPF, with an inverse relationship existing between SAA concentrations and lung capacity [44]. We also highlighted the Serpina3 family, ceruloplasmin (Cp) and haptoglobin (Hp), which are all involved in the acute phase of inflammation and are upregulated in PF [45–47]. Similar results were obtained for cytokines, such as the chemoattractant Ccl2, which promotes the differentiation of fibrocytes into fibroblasts, thus inducing excessive collagen production [48]. Other chemo-attractants, such as Cxcl1 and Cxcl13, stimulate the recruitment of immune cells to the lung parenchyma [49]. Lastly, several genes encoding complement proteins were also upregulated in our condition with induced fibrosis. The complement system is an integral part of the innate immune system and plays an important role in inflammation and tissue regeneration; moreover, it has been reported that the depletion of serum complement in a bleomycin-induced PF mouse model was highly effective in inhibiting lung collagen deposition [50]. Therefore, our transcriptomics data demonstrated that our model of induced fibrosis recapitulates many of the characteristic pathways of PF.

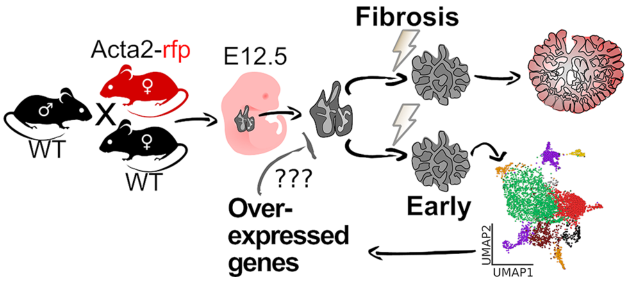

Fig. 9 Schematic overview of the study. Mouse embryonic lung explant culture can be used to mimic fibrosis and identify target genes for new therapeutic approaches among all of the early upregulated genes

Interestingly, the transcriptomics analysis revealed that, among the 112 genes that were most upregulated in the pro-fibrosis condition, five are associated with metal ion homeostasis. These genes were *Mt2*, *Lcn2*, *Steap4*, *Cp* and *Sod2*, all of which are involved in iron metabolism. Studies highlighting the link between ferroptosis, which defines a dysfunction of iron metabolism, and PF are abundant in the scientific literature. This deregulation of iron metabolism induces an increase in the level of reactive oxygen derivatives, which promotes the development of PF [51].

In conclusion, we presented here a novel and original experimental model of PF. The administration of a pro-fibrotic cocktail triggered fibrosis, as manifested by the histological evidence of fibrosis at several days after treatment. This model should offer an easy way of testing fibrosis inhibitors with inhibitors of gene overexpression, using anti-sense oligonucleotides or anti-sense RNA, for example, or with antibodies or drugs (Fig. 9). An early transcriptomics analysis revealed the overexpression of genes and gene families associated with inflammation, fibrosis and ferroptosis. Several of the genes identified here have not previously been linked to the development of PF. These genes could emerge as potential new therapeutic targets, by decreasing their expression levels. These targets could be validated upstream on a model of induced fibrosis, using thick sections from cultured adult mouse, pig or human lungs.

Supplementary Information The online version contains supplementary material available at https://doi.org/10.1007/s00018-025-05620-0.

Acknowledgements We thank J. Devassine (Animal Core Facility, UMS 2014 – US 41 – PLBS/Plateformes Lilloise en Biologie et Santé), and M-H. Gevaert (UMS 2014 – US 41 – PLBS) for the histological sections, M. Tardivel and A. Bongiovanni for cell imaging (BICeL, UMS 2014 – US 41 – PLBS), J-P Meneboo and M. Figeac for scRNAseq3′ (Go@L-GFS, UMS 2014 – US 41 – PLBS).

Author contributions Conceptualization: N.H., V.G. and J.-L.D. Experiments: N.H., V.G. and L.V. Analysis: N.H., V.G., J.-L.D. S.H. and

C.C. scRNAseq3′ analysis, C.B. Writing: N.H., V.G. F.G. and J.-L.D. Review & Editing: all authors.

Funding This work was supported by the «1000 days for health» program (FHU from Univ. Lille) and the CHU of Lille and the Région Hauts de France (NH PhD fellowship).

Data availability Original datasets of single-cell RNA-sequencing, analysis R scripts and code for the interactive 3D representations of the UMAP superposition are available in the Zenodo repository, https://doi.org/10.5281/zenodo.13285840. Interactive 3D representations of the UMAP superposition for the two conditions PBS vs. fibrosis cocktail, without or with cell clustering are available at https://cbedart.github.io/scRNAseq/Hennion2024/UMAP_Conditions/ and https://cbedart.github.io/scRNAseq/Hennion2024/UMAP_Celltypes/, respectively. A 3D UMAP representation grouping both conditions and cell types is available at https://cbedart.github.io/scRNAseq/Hennion2024/UMAP_Celltypes_Conditions/. The interactive volcano plot can be accessed via the URL: https://cbedart.github.io/scRNAseq/Hennion2024/VolcanoPlot/. Other data are available within the article or are available from the corresponding author on reasonable request.

Declarations

Ethics approval The animal protocols were in accordance with the French Guide for the Care and Use of Laboratory Animals and with the guidelines of the European Union. Animal housing and all experimental procedures were approved by and performed according to the National Institutional Animal Ethics Committees and institutional guidelines (APAFIS#25481-2020050415255797 v4).

Competing interests Author SH and CC declare they have no financial interests. SH declares personal fees from Boehringer-Ingelheim, Merck & Co, Bristol Myers Squibb. CC declares grants from AstraZeneca, GSK, Novartis, Santelys, personal fees from ALK-Abello, AstraZeneca, Boehringer-Ingelheim, Chiesi, GSK, Sanofi and congress support from AstraZeneca, Boehringer-Ingelheim, Chiesi, Novartis, Sanofi. Other authors have no relevant financial or non-financial interests to disclose.

References

1. Travis WD, Costabel U, Hansell DM et al (2013) An official American thoracic society/European respiratory society statement: update of the international multidisciplinary classification of the idiopathic interstitial pneumonias. Am J Respir Crit Care Med 188:733–748. https://doi.org/10.1164/rccm.201308-1483ST
2. Hilberg O, Hoffmann-Vold A-M, Smith V et al (2022) Epidemiology of interstitial lung diseases and their progressive-fibrosing behaviour in six European countries. ERJ Open Res 8:00597–02021. https://doi.org/10.1183/23120541.00597-2021
3. Martinez FJ, Collard HR, Pardo A et al (2017) Idiopathic pulmonary fibrosis. Nat Rev Dis Primer 3:17074. https://doi.org/10.1038/nrdp.2017.74
4. Kang HK, Song JW (2024) Progressive pulmonary fibrosis: where are we now?? Tuberc Respir Dis 87:123–133. https://doi.org/10.4046/trd.2023.0119
5. Copeland CR, Collins BF, Salisbury ML (2021) Identification and remediation of environmental exposures in patients with interstitial lung disease: evidence review and practical considerations. Chest 160:219–230. https://doi.org/10.1016/j.chest.2021.02.021
6. Blanc PD, Annesi-Maesano I, Balmes JR et al (2019) The occupational burden of nonmalignant respiratory diseases. An official American thoracic society and European respiratory society statement. Am J Respir Crit Care Med 199:1312–1334. https://doi.org/10.1164/rccm.201904-0717ST
7. Dsouza KG, Alexander AS, Watts JR, Kulkarni T (2023) Management of interstitial lung disease in patients with autoimmune disease-related interstitial lung disease. Multidiscip Respir Med 18:890. https://doi.org/10.4081/mrm.2023.890
8. Borie R, Le Guen P, Ghanem M et al (2019) The genetics of interstitial lung diseases. Eur Respir Rev Off J Eur Respir Soc 28:190053. https://doi.org/10.1183/16000617.0053-2019
9. Tsakiri KD, Cronkhite JT, Kuan PJ et al (2007) Adult-onset pulmonary fibrosis caused by mutations in telomerase. Proc Natl Acad Sci U S A 104:7552–7557. https://doi.org/10.1073/pnas.0701009104
10. Torres PPTES, Rabahi MF, Moreira MAC et al (2017) Usual interstitial pneumonia: typical, possible, and inconsistent patterns. J Bras Pneumol 43:393–398. https://doi.org/10.1590/S1806-37562016000000368
11. de Lauretis A, Veeraraghavan S, Renzoni E (2011) Review series: aspects of interstitial lung disease: connective tissue disease-associated interstitial lung disease: how does it differ from IPF? How should the clinical approach differ? Chron Respir Dis 8:53–82. https://doi.org/10.1177/1479972310393758
12. Phan SH (2012) Genesis of the myofibroblast in lung injury and fibrosis. Proc Am Thorac Soc 9:148–152. https://doi.org/10.1513/pats.201201-011AW
13. Suga M, Iyonaga K, Ichiyasu H et al (1999) Clinical significance of MCP-1 levels in BALF and serum in patients with interstitial lung diseases. Eur Respir J 14:376–382. https://doi.org/10.1034/j.1399-3003.1999.14b23.x
14. Kolahian S, Fernandez IE, Eickelberg O, Hartl D (2016) Immune mechanisms in pulmonary fibrosis. Am J Respir Cell Mol Biol 55:309–322. https://doi.org/10.1165/rcmb.2016-0121TR
15. Del Moral PM, Warburton D (2010) Explant culture of mouse embryonic whole lung, isolated epithelium, or mesenchyme under chemically defined conditions as a system to evaluate the molecular mechanism of branching morphogenesis and cellular differentiation. Methods Mol Biol 633:71–79. https://doi.org/10.1007/978-1-59745-019-5_5
16. Alsafadi HN, Staab-Weijnitz CA, Lehmann M et al (2017) An ex vivo model to induce early fibrosis-like changes in human precision-cut lung slices. Am J Physiol Lung Cell Mol Physiol 312:L896–L902. https://doi.org/10.1152/ajplung.00084.2017
17. Hu X, Fernandes J, Jones DP, Go Y-M (2017) Cadmium stimulates myofibroblast differentiation and mouse lung fibrosis. Toxicology 383:50–56. https://doi.org/10.1016/j.tox.2017.03.018
18. Lee CG, Homer RJ, Zhu Z et al (2001) Interleukin-13 induces tissue fibrosis by selectively stimulating and activating transforming

growth factor beta(1). J Exp Med 194:809–821. https://doi.org/10.1084/jem.194.6.809

19. Gouyer V, Leir S-H, Tetaert D et al (2010) The characterization of the first anti-mouse Muc6 antibody shows an increased expression of the mucin in pancreatic tissue of Cftr-knockout mice. Histochem Cell Biol 133:517–525. https://doi.org/10.1007/s00418-010-0688-8
20. Valque H, Gouyer V, Husson M-O et al (2011) Abnormal expression of Muc5b in Cftr-null mice and in mammary tumors of MMTV-ras mice. Histochem Cell Biol 136:699–708. https://doi.org/10.1007/s00418-011-0872-5
21. Ashcroft T, Simpson JM, Timbrell V (1988) Simple method of estimating severity of pulmonary fibrosis on a numerical scale. J Clin Pathol 41:467–470. https://doi.org/10.1136/jcp.41.4.467
22. Ségard B-D, Kimura K, Matsuoka Y et al (2024) Quantification of fibrosis extend and airspace availability in lung: A semi-automatic ImageJ/Fiji toolbox. PLoS ONE 19:e0298015. https://doi.org/10.1371/journal.pone.0298015
23. Portal C, Gouyer V, Gottrand F, Desseyn J-L (2017) Preclinical mouse model to monitor live Muc5b-producing conjunctival goblet cell density under Pharmacological treatments. PLoS ONE 12:e0174764. https://doi.org/10.1371/journal.pone.0174764
24. Lacroix G, Gouyer V, Rocher M et al (2022) A porous cervical mucus plug leads to preterm birth induced by experimental vaginal infection in mice. iScience 25:104526. https://doi.org/10.1016/j.isci.2022.104526
25. Germain P-L, Lun A, Garcia Meixide C et al (2021) Doublet identification in single-cell sequencing data using ScDblFinder. F1000Research 10:979. https://doi.org/10.12688/f1000research.73600.2
26. Ianevski A, Giri AK, Aittokallio T (2022) Fully-automated and ultra-fast cell-type identification using specific marker combinations from single-cell transcriptomic data. Nat Commun 13:1246. https://doi.org/10.1038/s41467-022-28803-w
27. Negretti NM, Plosa EJ, Benjamin JT et al (2021) A single-cell atlas of mouse lung development. Dev Camb Engl 148:dev199512. https://doi.org/10.1242/dev.199512
28. Kolanko E, Cargnoni A, Papait A et al (2024) The evolution of in vitro models of lung fibrosis: promising prospects for drug discovery. Eur Respir Rev 33:230127. https://doi.org/10.1183/16000617.0127-2023
29. Yanagihara T, Chong SG, Vierhout M et al (2020) Current models of pulmonary fibrosis for future drug discovery efforts. Expert Opin Drug Discov 15:931–941. https://doi.org/10.1080/17460441.2020.1755252
30. Carrington R, Jordan S, Pitchford SC, Page CP (2018) Use of animal models in IPF research. Pulm Pharmacol Ther 51:73–78. https://doi.org/10.1016/j.pupt.2018.07.002
31. Schruf E, Schroeder V, Le HQ et al (2020) Recapitulating idiopathic pulmonary fibrosis related alveolar epithelial dysfunction in a human iPSC-derived air-liquid interface model. FASEB J 34:7825–7846. https://doi.org/10.1096/fj.201902926R
32. Gauldie J, Sime PJ, Xing Z et al (1999) Transforming growth factor-beta gene transfer to the lung induces myofibroblast presence and pulmonary fibrosis. Curr Top Pathol Ergeb Pathol 93:35–45. https://doi.org/10.1007/978-3-642-58456-5_5
33. Bonner JC (2004) Regulation of PDGF and its receptors in fibrotic diseases. Cytokine Growth Factor Rev 15:255–273. https://doi.org/10.1016/j.cytogfr.2004.03.006
34. Kolb M, Margetts PJ, Anthony DC et al (2001) Transient expression of IL-1beta induces acute lung injury and chronic repair leading to pulmonary fibrosis. J Clin Invest 107:1529–1536. https://doi.org/10.1172/JCI12568
35. Yi ES, Wawryko P, Ryu JH (2024) Diagnosis of interstitial lung diseases: from Averill A. Liebow to artificial intelligence. J Pathol Transl Med 58:1–11. https://doi.org/10.4132/jptm.2023.11.17
36. Marchal-Duval E, Homps-Legrand M, Froidure A et al (2023) Identification of Paired-related homeobox protein 1 as a key mesenchymal transcription factor in pulmonary fibrosis. eLife 12:e79840. https://doi.org/10.7554/eLife.79840
37. Chen L-J, Ye H, Zhang Q et al (2015) Bleomycin induced epithelial-mesenchymal transition (EMT) in pleural mesothelial cells. Toxicol Appl Pharmacol 283:75–82. https://doi.org/10.1016/j.taap.2015.01.004
38. Shih AR, Nitiwarangkul C, Little BP et al (2021) Practical application and validation of the 2018 ATS/ERS/JRS/ALAT and Fleischner society guidelines for the diagnosis of idiopathic pulmonary fibrosis. Respir Res 22:124. https://doi.org/10.1186/s12931-021-01670-7
39. Carmo-Fernandes A, Puschkarow M, Peters K et al (2021) The pathogenic role of smooth muscle Cell-Derived Wnt5a in a murine model of lung fibrosis. Pharm Basel Switz 14:755. https://doi.org/10.3390/ph14080755
40. Wiesemann A, Ketteler J, Slama A et al (2019) Inhibition of Radiation-Induced Ccl2 signaling protects lungs from vascular dysfunction and endothelial cell loss. Antioxid Redox Signal 30:213–231. https://doi.org/10.1089/ars.2017.7458
41. Costa PM, Gosens I, Williams A et al (2018) Transcriptional profiling reveals gene expression changes associated with inflammation and cell proliferation following short-term inhalation exposure to copper oxide nanoparticles. J Appl Toxicol 38:385–397. https://doi.org/10.1002/jat.3548
42. Curras-Alonso S, Soulier J, Defard T et al (2023) An interactive murine single-cell atlas of the lung responses to radiation injury. Nat Commun 14:2445. https://doi.org/10.1038/s41467-023-38134-z
43. Habermann AC, Gutierrez AJ, Bui LT et al (2020) Single-cell RNA sequencing reveals profibrotic roles of distinct epithelial and mesenchymal lineages in pulmonary fibrosis. Sci Adv 6:eaba1972. https://doi.org/10.1126/sciadv.aba1972
44. Vietri L, Bennett D, Cameli P et al (2019) Serum amyloid A in patients with idiopathic pulmonary fibrosis. Respir Investig 57:430–434. https://doi.org/10.1016/j.resinv.2019.03.010
45. Gong G-C, Song S-R, Xu X et al (2020) Serpina3n is closely associated with fibrotic procession and knockdown ameliorates bleomycin-induced pulmonary fibrosis. Biochem Biophys Res Commun 532:598–604. https://doi.org/10.1016/j.bbrc.2020.08.094
46. Carleo A, Bargagli E, Landi C et al (2016) Comparative proteomic analysis of Bronchoalveolar lavage of Familial and sporadic cases of idiopathic pulmonary fibrosis. J Breath Res 10:026007. https://doi.org/10.1088/1752-7155/10/2/026007
47. Saraswat M, Joenväärä S, Tohmola T et al (2020) Label-free plasma proteomics identifies haptoglobin-related protein as candidate marker of idiopathic pulmonary fibrosis and dysregulation of complement and oxidative pathways. Sci Rep 10:7787. https://doi.org/10.1038/s41598-020-64759-x
48. Moore BB, Kolodsick JE, Thannickal VJ et al (2005) CCR2-mediated recruitment of fibrocytes to the alveolar space after fibrotic injury. Am J Pathol 166:675–684. https://doi.org/10.1016/S0002-9440(10)62289-4
49. Komolafe K, Pacurari M (2022) CXC Chemokines in the Pathogenesis of Pulmonary Disease and Pharmacological Relevance. Int J Inflamm 2022:4558159. https://doi.org/10.1155/2022/4558159
50. Phan SH, Thrall RS (1982) Inhibition of bleomycin-induced pulmonary fibrosis by Cobra venom factor. Am J Pathol 107:25–28

51. Huang X, Song Y, Wei L et al (2023) The emerging roles of ferroptosis in organ fibrosis and its potential therapeutic effect. Int Immunopharmacol 116:109812. https://doi.org/10.1016/j.intimp.2023.109812